Journal of X-Ray Science and Technology 23 (2015) 229–241
DOI 10.3233/XST-150483
IOS Press

A prior-based metal artifact reduction algorithm for x-ray CT

Ming Li[a,b,c], Jian Zheng[c,*], Tao Zhang[a], Yihui Guan[d], Pin Xu[c] and Mingshan Sun[c]
[a]*Changchun Institute of Optics, Fine Mechanics and Physics, Chinese Academy of Sciences, Changchun, Jilin, China*
[b]*University of Chinese Academy of Sciences, Beijing, China*
[c]*Medical Imaging Department, Suzhou Institute of Biomedical Engineering and Technology, Chinese Academy of Sciences, Suzhou, Jiangsu, China*
[d]*PET Center, Huashan Hospital, Fudan University, Shanghai, China*

Received 22 June 2014
Revised 7 December 2014
Accepted 7 January 2015

Abstract. In computed tomography (CT), metal objects in the scanning filed are accompanied by physical phenomenon that causes projections to be inconsistent. These inconsistencies produce bright and dark shadows or streaks in analytically reconstructed images. Interpolation-based metal artifact reduction (MAR) algorithms usually replace the inconsistent projection data by estimating surrogate data based on the surrounding uncorrupted projections. In such cases, secondary artifacts will be generated when the data estimates are inaccurate. Therefore, better projection estimation is critical. This paper proposes an image post-processing strategy to create an intermediate image, named the prior image and better estimates of the surrogate data by forward projecting this prior image. The proposed method consists of three steps based on the forward projection MAR framework. First, metallic implants in the uncorrected images are segmented using a Markov random field model (MRF). Then a prior image is generated via an edge-preserving filter and a recovery procedure of the adjacent anatomical structures. Finally, the projection is completed via forward projecting this prior image and the corrected image is reconstructed by the filtered backprojection (FBP) method. Studies on both phantom and clinical data are carried out to verify the performance of the proposed method. The comparisons with other previous MAR algorithms demonstrate that the proposed MAR method performs better in metal artifact suppression and anatomical structure preservation.

Keywords: Computed tomography, metal artifact reduction, secondary artifacts, prior image

1. Introduction

In the past decades, x-ray computed tomography has been widely used in clinical diagnosis. Modern clinical CT now can produce high-resolution images with reliable anatomical information. However, if metal implants (such as prosthetic devices or dental fillings) are present in the field of scan, streaks and dark or bright shadows will appear in the images of filtered backprojection (FBP) based reconstruction. These artifacts often deteriorate the quality of the reconstructed images and lower their diagnosis value,

*Corresponding author: Jian Zheng, Medical Imaging Department, Suzhou Institute of Biomedical Engineering and Technology, Chinese Academy of Sciences, Suzhou 215163, Jiangsu, China. E-mail: zhengj@sibet.ac.cn.

making it difficult for radiologists to accurately interpret the CT images [1,2]. The problem has existed for many years, and various metal artifact reduction (MAR) algorithms have been proposed. They can be roughly classified into sinogram in-painting methods [1–11], iterative methods [12–15], and hybrid methods [16–19].

Iterative methods and hybrid methods are usually less susceptible to metal artifacts, and have shown good performance in metal artifacts suppression. However, the clinical potential of these methods is limited due to their high computational cost. Sinogram in-painting based methods, which are the most common MAR methods, usually estimate the surrogate data using various interpolation techniques. In the sinogram in-painting methods, the original sinogram is corrected by replacing metal-affected data in the metal shadow with surrogate data, which are generally obtained from interpolation or forward projection of prior images. The first step is to identify the corrupted projection data caused by metal objects. To achieve this goal, an uncorrected image is first reconstructed from the raw sinogram data. Then various image segmentation methods are used to identify the metal parts in the image domain. Forward projection of the metal-only image is used to determine the metal trace in the raw sinogram. After that, a correction step is implemented to estimate the surrogate data in the metal trace. Correction methods can be roughly classified into two groups: interpolation-based methods [1–6] and prior image [7–11] based methods.

Among various interpolation-based methods, linear interpolation (LI) is the simplest way to achieve that. We refer it to LI-MAR [2,3] in this work. In LI-MAR methods, the missing projections are estimated via linear interpolation using projections surrounding the metal trace. LI-MAR method is usually computationally efficient. However, due to unavoidable inaccurate estimation, it often generates secondary artifacts and leads to loss of anatomical structure in the vicinity of metallic objects. Prior image based methods are intended to build a prior image, which is sufficiently similar to the metal-free image. In prior-based MAR methods, the metal traces are estimated via the forward projection of a prior image, which can achieve good results as long as the prior image is close enough to the metal-free image. However, most existing methods, such as those given by Prell et al. [9] and Meyer et al. [8], build the prior images by segmenting the originally reconstructed image (the uncorrected image) or the precorrected image (via interpolation-based MAR) into air, soft-tissue and bone equivalent materials. We will call them the thresholded-prior methods (TP-MAR) in this work. One main limitation is that wrong segmentation remains unavoidable, which will lead to residual artifacts and loss of some soft-tissue structure details. Therefore, to build a good prior image is the core step in the prior-based MAR methods. Recently, a hybrid metal artifact reduction algorithm [19] was developed. This method first pre-processed the uncorrected image to generate an initial prior image. Then, it was used as the initial image of iterative reconstruction to produce a better prior image. The experiments on the head CT scans described in Ref. [19] had shown that this method could produce more accurate prior images than the TP-MAR methods, and could provide better image quality than both the LI-MAR and TP-MAR methods. However, pre-correction and TV minimization constrained reconstruction still need long computational time. Hence, a novel, efficient prior-based metal artifact reduction algorithm is proposed in this work.

2. Methods

The proposed MAR method adopts a framework similar to other MAR methods based on forward projecting a prior image, while the prior image is obtained via an image post-processing strategy. The new approach consists of three main steps: 1) segmentation of metal object, 2) generation of prior image, 3) sinogram completion and FBP reconstruction. The scheme of the proposed prior-based MAR algorithm is as depicted in Fig. 1.

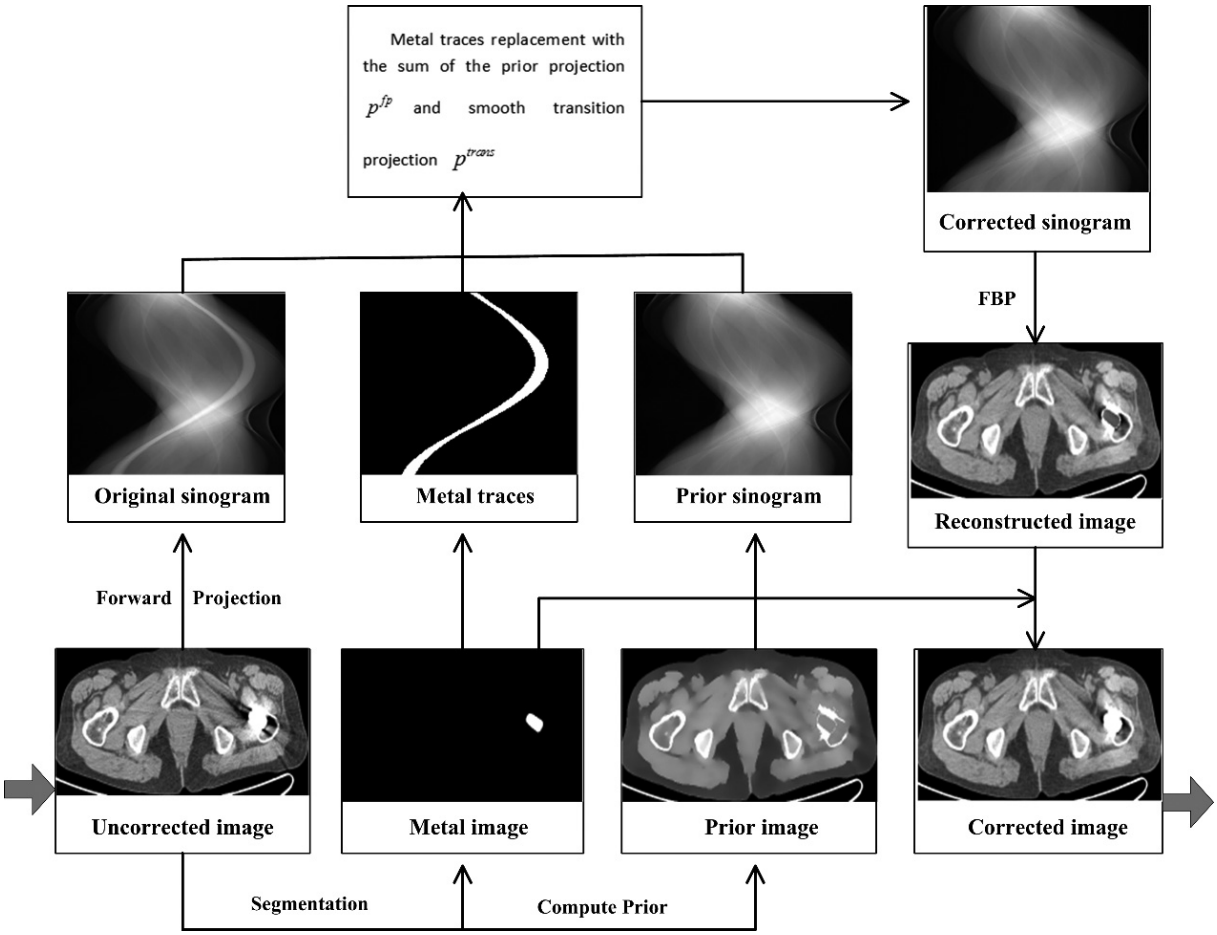

Fig. 1. Scheme of the proposed MAR method. By MRF model, the uncorrected image is segmented to acquire metal image and the prior image is obtained via image post-processing technique. Forward projection yields the corresponding sinogram. The metal traces determine where data in original sinogram are replaced by interpolation. FBP reconstruction and metal implantation yield the corrected image.

2.1. Segmentation of the metal implant

In this part, we will extract metal only image from original uncorrected CT image. In order to acquire accurate boundaries of metallic implant, a Markov random field (MRF) model [5,20,21] in combination with Bayesian techniques is applied to obtain the final optimized segmentation result. The MRF model is specified by labeling a pixel on the basis of the conditional probability distribution, given its gray level and labels of its neighbors. Due to that the MRF model considers not only the fluctuation of the pixel value but also the interaction with its neighborhood labels, the MRF model can obtain better segmentation result compared to simple threshold segmentation. In this approach, we aim at finding a solution that maximizes the posteriori probability density of x given y, which according to Bayes' rule is given by

$$P(X = x|Y = y) \propto P(Y = y|X = x)P(X = x), \tag{1}$$

where r.h.s densities are the probability density of y given x, and the prior probability density of x, respectively. In practice, suitable models for $P(Y|X)$ and $P(X)$ have to be adopted in order to maximize

the posteriori probability of X given Y. If conditional independence and Gaussian distribution of y_i given x_i are assumed, then we have

$$\begin{aligned} P(Y = y|X = x) &= \prod_i P(y_i|x_i = l) \\ &= \prod_i \frac{1}{\sqrt{2\pi}\sigma_l} \exp\left(-\frac{(y_i - \mu_l)^2}{2\sigma_l^2}\right), \end{aligned} \tag{2}$$

where μ_l and σ_l are the mean and variance for a given class l. In this framework, a Markov random field is used as a model for $P(X)$. The prior probability distribution corresponding to a MRF can be expressed in the following form:

$$\begin{aligned} P(X = x) &= \frac{1}{Z} \exp\left(-U(x)\right) \\ &\propto \exp\left[-\sum_{l=1}^{K} \beta_l g(l)\right], \end{aligned} \tag{3}$$

where $U(x)$ is Gibbs or prior energy, β is used for modeling the priori likelihood of the neighborhood labels to occur. $g(l)$ is the number of neighbors with class l and K is the number of classes. The maximum a posteriori (MAP) estimation is then obtained by maximizing $P(X|Y)$, or equivalently minimizing the following posteriori energy:

$$\begin{aligned} \hat{x} &= \arg\min u(x_i = l|(y_i, \text{ other labels})) \\ &= \arg\min \left\{ \sum_i \frac{(y_i - u_l)^2}{2\sigma_l^2} + \log\sqrt{2\pi}\sigma_l + \beta_l g(l) \right\}. \end{aligned} \tag{4}$$

In the above equation, u represents posterior energy function, x_i stands for the label of pixel i, which takes only one of the two values ($l = 1$, stand for foreground; $l = 0$, stand for background, respectively), and y_i represents the pixel value of pixel i. The interaction parameter β was set to 0 with $l = 1$ and was set to 7 with $l = 0$ [5]. The neighbors used here consists 24 pixels in a 5×5 window centered at site i.

The proposed MRF model needs an initial estimate of the labeling. In our tests, initial segmentation result is acquired by applying region growing methods, which can provide an initial distribution of the labeling. Then, these labeling results are updated iteratively. In each iteration, a pixel is marked with the label that gives the minimum posterior energy according to formula (4), where μ_l, σ_l and $g(l)$ are adjusted before every new iteration step. We implemented ten iterations since the segmentation converges within ten iterations. The final segmentation result is shown in Fig. 2(b).

2.2. Generation of prior image

In this section, we aim at producing a prior image (intermediate image) by processing the originally reconstructed image. First, the CT values of metal parts in uncorrected image are set to 50 HU (soft-tissue CT value) according to the above-mentioned segmentation result. Then, an edge-preserving filter is selected to suppress streak artifact in the originally uncorrected image. Finally, we delete any dark and bright shadow areas and restore anatomical structures adjacent to the metal object to generate the ultimate prior image.

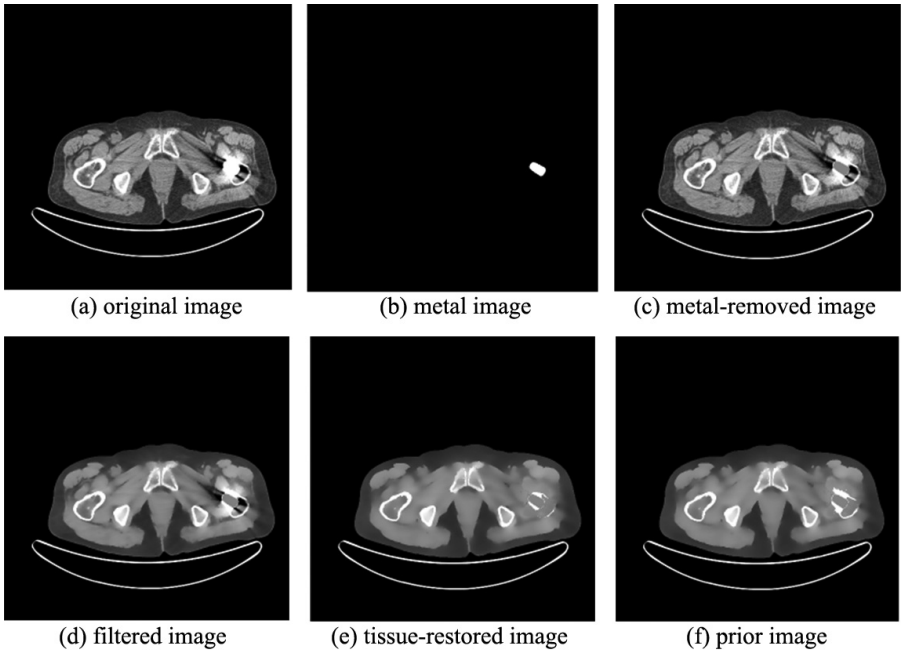

Fig. 2. Stages flow in the generation of a prior image of a hip CT scan. The uncorrected image is shown in (a) and the metallic implant segmentation result is in (b), and the metal-removed image is shown in (c). Result of edge-preserving filter and the recovery of adjacent tissue labels are depicted in (d), (e) respectively. And the final prior image is in (f). Window settings: WW/WL 400/0 HU.

2.2.1. Edge-preserving filter

In this step, we propose an edge-preserving filter to suppress streak artifacts in the originally uncorrected image with metallic implants removed. Given an original artifacts image $v = \{v(i) \,|i \in I\}$, each value $v_{AF}(i)$ in the filtered image is the weighted average of pixels within a local square region around the pixel i:

$$v_{AF}(i) = \sum_{i \in I, j \in N_i} w(i,j) v(j), \tag{5}$$

where the family of $w(i,j)$ depend on the similarity between the pixel i and j, and this similarity is measured as a decreasing function of the weighted Euclidean distance. To preserve tissues edges, a user-defined threshold is proposed to guarantee that only those pixels with CT value similar to the center pixel are contributing to the average. The weights are defined as:

$$w(i,j) = \begin{cases} \dfrac{1}{Z(i)} e^{-\frac{\|v(i)-v(j)\|_2^2}{h^2}} & |v(i) - v(j)| \leqslant T \\ 0 & |v(i) - v(j)| > T \end{cases}, \tag{6}$$

where $Z(i)$ is the normalization factor:

$$\begin{aligned} Z(i) &= \sum_{j \in N_i} e^{-\frac{\|v(i)-v(j)\|_2^2}{h^2}} \cdot \chi(|v(i) - v(j)| - T) \\ \chi(x) &= \begin{cases} 1 & x \leqslant 0 \\ 0 & \text{others} \end{cases} \end{aligned}, \tag{7}$$

where T is a threshold for the identification of the similar pixels, h is a parameter controlling the extent of filtering; N is the size of filtering window. T, N and h should be properly selected to achieve artifacts suppression without blurring the edges between air, soft tissue and bones. Figure 2(d) illustrates that the streak artifacts in Fig. 2(c) are well suppressed and better clear tissue structure are achieved compared to Fig. 2(c). In our tests, $T = 60$ HU, $N = 20$ and $h = 10$ can lead to good results for all the cases studied in this work. The above values are determined via experimental results, but we do not guarantee them to be optimal. However, the test results below demonstrate that the above parameters are satisfactory.

2.2.2. Removal of dark and bright artifacts

In this step, based on the previous filtered result, we aim at producing the final prior image by removing the dark and bright artifacts in the neighborhood of metal parts. Due to the influence of dark and bright artifacts, soft tissue pixels adjacent to metal objects are severely contaminated. Therefore, removal of dark and bright artifacts and recovery of adjacent anatomical structures is the key to the final prior image. However, if part of the bright artifacts grows into bone, the bone structure would be severely destroyed during the removal of the positive artifact region. Hence, before the recovery of the soft tissue values, we first adopt a threshold technique to extract the bone structure information from the previous filtered image, where the threshold window used here is 200 to 900 HU. Then, region growing is performed to identify the artifacts. For the MAR methods presented in Ref. [7], all soft tissue pixels are replaced with the mean value of these pixels, which may lead to artificial edges between soft tissue and other tissue structures, or even worse, false structures may appear in the prior image. Therefore, in order to avoid this drawback, a smooth transition between the soft tissue and other tissue types is necessary. We exploit a function of distance from metal, and the soft tissue pixels are assigned via the following formula (8):

$$f_i(D) = MIN_{soft} + Ae^{(-cD)}, \tag{8}$$

where D indicates the Euclidean distance between pixel i and its nearest metal pixel; MIN_{soft} denotes the minimal intensity value of the artifacts surrounding the metal; A is the amplitude of soft tissue values; c is a curve parameter, regulating the fluctuation of the reassigned soft tissue values. All values were determined empirically, $MIN_{soft} = -50 \sim 0$ HU, $A = 120$ HU and $c = 0.02$ can achieve good results for all cases.

Finally, bony information obtained by the means of threshold technique is superimposed on the tissue-restored image to generate the final prior image. The final prior image is shown in Fig. 2(f).

2.3. Sinogram completion and image reconstruction

In this step, the prior image as shown in Fig. 2(f) is forward projected to generate a prior sinogram to be used for the completion of the surrogate projection data. The metal trace is determined via calculation of the rays passing through the metal image and the ray-driven method used here is described in Ref [22]. However, if we replace the metal trace pixels with the corresponding ones of the prior sinogram directly, it may lead to new discontinuities at the boundaries of the metal traces. Therefore, elimination of the discontinuities is a significant step to achieve a relatively smooth corrected sinogram. In this work, we use the interpolation method proposed in Ref [19] for data replacement. This interpolation method is intended to produce a projection vector p^{trans} which is treated as a smooth transition between the uncorrected projection dataset p and the prior-image based projection dataset p^{fp}. For each view, we

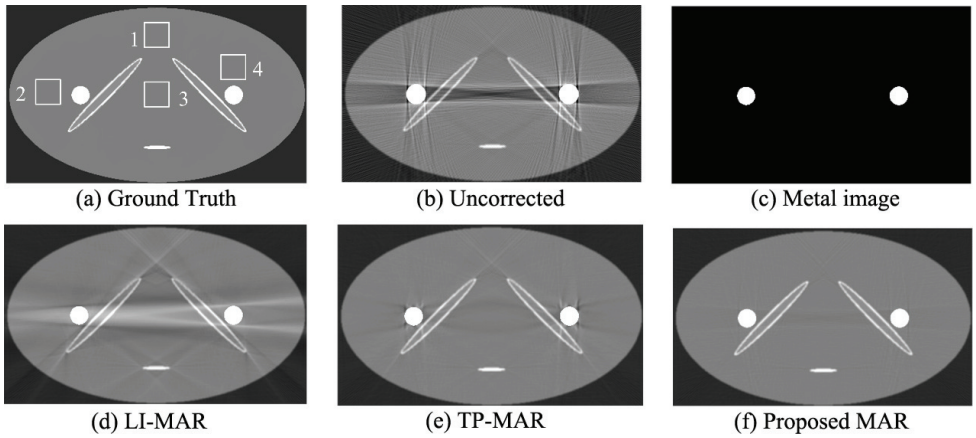

Fig. 3. Correction results comparison between the proposed and other MAR algorithms for the simulated hip phantom. Window settings: WW/WL = 2000/0 HU.

define $\{p_k|k \in [j+1, j+\Delta]\}$ as the metal trace and p_j, $p_{j+\Delta+1}$ are the neighboring projections unaffected by metal. Then the corrected sinogram p^{corr} can be obtained by formula (9),

$$\begin{aligned} p_k^{trans} &= (p_j - p_j^{fp}) + \frac{(p_{j+\Delta+1} - p_{j+\Delta+1}^{fp}) - (p_j - p_j^{fp})}{\Delta + 1}(k - j) \\ p^{corr} &= \begin{cases} p_k^{fp} + p_k^{trans} & \text{if } k \in [j+1, j+\Delta] \\ p & \text{others} \end{cases} \end{aligned} . \tag{9}$$

Finally, the artifact-reduced image is reconstructed via the conventional FBP algorithm and the segmented metal objects in the first step are superimposed on the corrected image to indicate the metallic implants.

3. Experiments and results

The proposed MAR method was first applied to simulated data. A digital hip phantom with bilateral prostheses was designed to generate simulated CT images. In order to simulate beam hardening and the streaking artifacts from the metal, we modeled the polychromatic propagation of x-ray beams through the bilateral hip phantom, according to the model presented in Ref [23]. An x-ray spectrum of 120 kVp was simulated via the model described in Ref [24]. The simulation was performed with the following settings, including 600 detector channels, 720 views per rotation, and 30 energy bins for the x-ray spectrum.

The proposed MAR method was then tested on actual CT images. As presented in Figs 4 and 5, seven clinical cases with metal artifacts from hip prostheses and dental fillings were selected to test the capability of our method. All the original uncorrected images, in DICOM format, were obtained from our collaborator in Huashan Hospital. For each case, the original sinogram was simulated by forward projecting the uncorrected image. The resolution of the CT images is 512 × 512 pixels and the size of the simulated sinograms is 1024 × 720 pixels (720 views per circle). All the CT images were processed by MATLAB R2011a, (The Math Works Inc., Natick, MA) on a PC workstation (Intel(R) Core(TM) Quad CPU 2.66 GHz processor and 2048 Mb RAM).

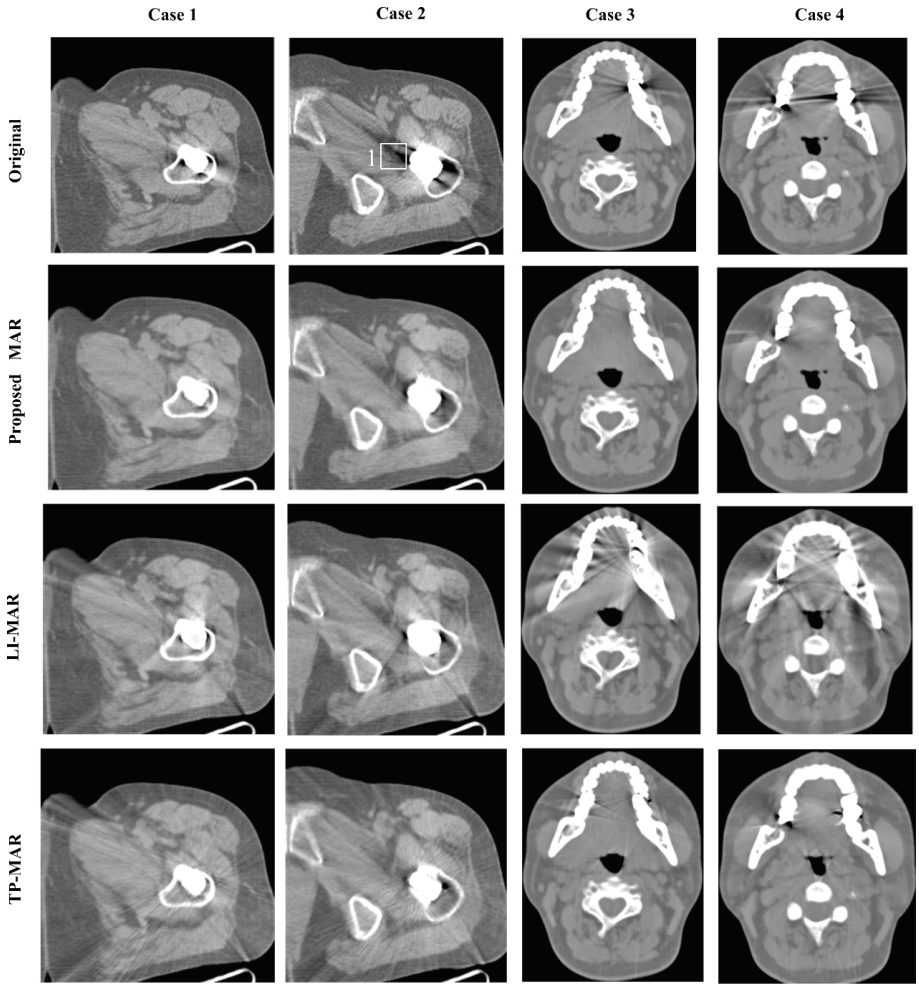

Fig. 4. Four sets of images are shown in columns. Each set contains the original, the proposed MAR, LI-MAR and TP-MAR corrected images. In all cases, the proposed post-processed prior corrections result in improvements over the original image, over LI-MAR, and over TP-MAR. Window settings: WW/WL = 600/0 HU for cases 1–2 and WW/WL = 1000/0 HU for cases 3–4.

The original uncorrected images and images corrected via our proposed MAR algorithm are shown in Figs 3–5. For comparison, results of LI-MAR (no prior image) and TP-MAR (a threshold prior image, using the same interpolation technique described in Section 2.3) are also shown. To generate the TP-MAR prior, we use tissue-class model described in Ref [7]. In that work, k-means clustering technique was applied to segment air, soft tissue, and bone after the image was smoothed via a Gaussian filter. Then, the air regions were set to -1000 HU, the soft tissue regions and metal parts were set to 0 HU, while bone pixels kept their original CT values. Finally, the interpolation method described above was used for data replacement in the metal traces. Since the interpolation technique and the segmented metallic implants were the same for all the MAR methods, the prior image was the key factor that determined the improvement.

Result from the simulated phantom study is illustrated in Fig. 3. We can see that the uncorrected image suffers from severe streaking artifacts between the metallic implants. In the LI-MAR result, significant

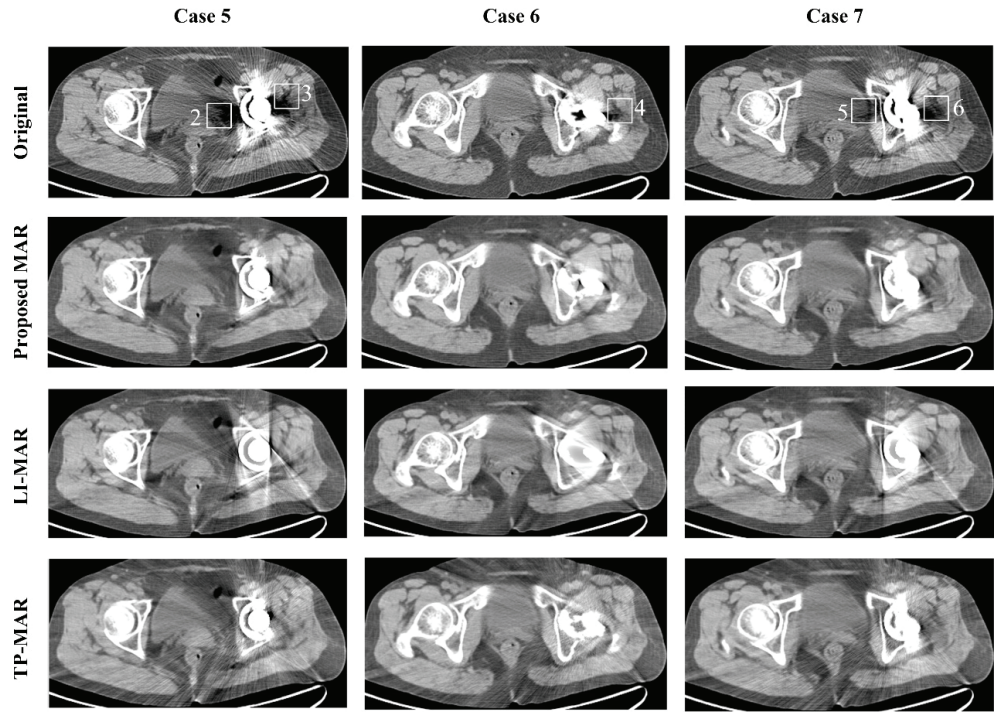

Fig. 5. Another three sets suffering from more severe metal artifacts, and the correction results are shown for cases 5–7. Window settings: WW/WL = 400/0 HU.

bright artifacts are introduced, and the secondary artifacts in LI-MAR processed image are even worse than the uncorrected one. When compared to LI-MAR, TP-MAR yields obviously improved image quality with the bright artifacts fully suppressed, but some residual artifacts are still remaining near the metallic implants. In comparison to LI-MAR and TP-MAR, the proposed MAR algorithm leads to the best image quality with no noticeable residual artifacts.

Clinical experiments show that artifacts are significantly removed by our proposed MAR algorithm even for multiple metal pieces (cases 4, 6), or for large metal pieces. Compared to the other two methods, our algorithm leads to the best image quality with fewest residual artifacts and finest bone structure. Figure 4 illustrates correction results with simple or small metallic implants. Just as shown in cases 1, 2, 3 and 4, significant streak artifacts tangent to metallic implants in uncorrected images are displayed. Many secondary streak-like artifacts remain when applying LI-MAR and TP-MAR corrections. Both LI-MAR and TP-MAR produce new artifacts comparable to the original metal artifacts. However, TP-MAR brings significant improvements in bone structure preservation. We can see in Fig. 4 that our proposed MAR method produces the best results in metal artifacts suppression and bone tissue preservation.

The most challenging cases are shown in Fig. 5. We can see that the original uncorrected images suffer from severe beam hardening artifacts and streak artifacts in the vicinity of the metallic implants. The LI-MAR method suppresses beam hardening artifacts at the cost of introducing more severe streak artifacts and losing bone structures near the metal objects. The quality of LI-MAR results is even worse than the quality of the uncorrected ones, which stems from the fact that large metal implants result in large metal trace region. This will lead to severe loss of edge structure information in metal trace via linear interpolation. In comparison to LI-MAR, TP-MAR performs better in anatomical structure preservation. However, there are still visible streak-like artifacts appearing around the metal objects in

Table 1
Mean CT number and the standard deviation for all the ROIs in Fig. 3

Phantom	Ground truth	Uncorrected	LI-MAR	TP-MAR	Proposed MAR
ROI 1	-3.8 ± 4.2	19.4 ± 67.0	42.6 ± 71.7	19.3 ± 32.3	2.66 ± 20.1
ROI 2	3.3 ± 3.6	-66.3 ± 174.8	159.8 ± 155.3	-15.6 ± 12.2	-1.7 ± 14.4
ROI 3	-7.5 ± 5.5	-160.0 ± 384.2	383.6 ± 186.2	-32.9 ± 25.5	-18.2 ± 18.8
ROI 4	-1.1 ± 2.8	120.8 ± 233.8	-63.5 ± 113.7	39.5 ± 68.6	7.2 ± 19.1

Table 2
Mean CT number and the standard deviation for all the ROIs in Figs 4 and 5

Cases	Background	Uncorrected	LI-MAR	TP-MAR	Proposed MAR
ROI 1	35.2 ± 40.9	-40.8 ± 96.6	71.6 ± 53.9	8.9 ± 60.5	19.2 ± 50.6
ROI 2	-10.2 ± 23.2	-175.8 ± 81.3	-45.4 ± 35.2	-60.7 ± 38.2	-39.8 ± 27.0
ROI 3	31.3 ± 45.6	-147.7 ± 155.9	27.6 ± 77.3	7.3 ± 66.3	14.8 ± 55.6
ROI 4	34.4 ± 28.8	-31.7 ± 96.0	40.6 ± 55.2	60.6 ± 44.2	37.3 ± 53.0
ROI 5	5.0 ± 28.9	-80.8 ± 48.0	-9.7 ± 32.0	-13.4 ± 34.6	-11.7 ± 29.0
ROI 6	-9.9 ± 26.0	-92.5 ± 70.4	3.9 ± 42.6	-1.4 ± 38.8	-7.7 ± 39.9

the TP-MAR processed images, which is owing to a misclassification in generation of the threshold prior image. Obviously, our proposed MAR algorithm performs better than LI-MAR and TP-MAR in metal artifacts suppression as well as in restoring anatomical structures close to metal implants. This is because our proposed method preserves more anatomical structures in the final prior image, which is closer to metal-free image (gold standard image) compared to the threshold based prior.

In order to obtain an objective assessment of these algorithms, several regions of interest (ROIs) are drawn on the area suffering from severe artifacts, as shown in Figs 3–5. The mean CT number and the standard deviation of each ROI (refer to Fig. 3) in each reconstructed image are summarized in Table 1. Overall, the proposed MAR has mean CT number that is closest to the ground truth and also has the minimum standard deviation in most ROIs. For Figs 4 and 5, the reference background ROI is defined on a region away from the dark artifacts in the uncorrected image [25]. Because it is far away from the dark artifacts, the background ROI is little affected by the metal artifacts and sees little change after correction. Therefore it is used as the reference background for all images including those after correction. Table 2 shows the mean CT number and the standard deviation of each ROI (refer to Figs 4 and 5) in the reconstructed images. The results show that all above-mentioned algorithms give rise to a closer mean CT value to background mean CT value compared to the uncorrected mean CT value, which demonstrate that all the LI-MAR, TP-MAR, and the proposed methods can lead to noticeable reduction of dark artifacts. However, our proposed algorithm has mean CT number that is closest to the background mean CT number and also has the minimal standard deviation in most ROIs, which shows that the proposed algorithm can more effectively reduce the artifacts in comparison to LI-MAR and TP-MAR algorithms.

4. Discussions

A TP-MAR prior is generated by segmenting the original uncorrected image into air, soft tissue and bone, in which misclassification of artifact pixels as bone or air cannot be avoided (see the regions indicated by the white dotted arrow in Fig. 6). Therefore, some TP-MAR methods [8] recommend a first-pass interpolation-based MAR to provide an image with less severe artifacts, so that thresholding of this precorrected image is more likely to produce a good prior image. However, the quality of precorrected image cannot be guaranteed, especially when multiple metal pieces or large metal implants are present.

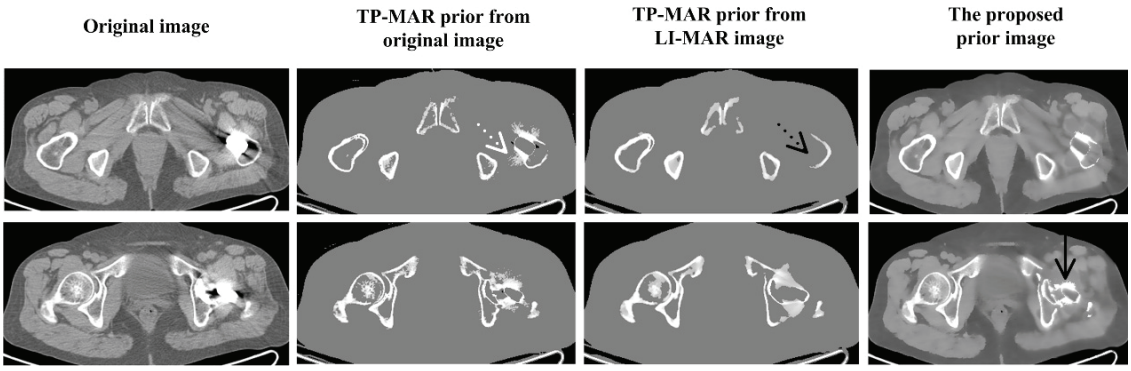

Fig. 6. Prior images illustration of TP-MAR and the proposed MAR method for the experiments with the hip prostheses (clinical Cases 2 and 6). TP-MAR prior images suffer from obvious segmentation errors, as indicated by the dotted arrows, errors may be produced in the final corrected images. The proposed post-processed prior images have higher quality with more anatomical structures information and less segmentation errors from artifacts.

Our experiments demonstrated that LI-MAR corrected results with metal artifacts may be compatible to or even worse than the original metal artifacts. Poor precorrected images undoubtedly yield poor prior images (see the regions indicated by the black dotted arrow in Fig. 6). TP-MAR prior image based on LI-MAR loses edge bone structures close to metal objects, thus large errors may be produced in the final corrected image. Furthermore, TP-MAR methods assume all the soft tissues have the same CT value. This hypothesis is far from the truth.

To overcome the defects of TP-MAR, an image post-processing strategy, based on the original uncorrected image, has been developed in this work to build a prior image with better quality. We first preserve anatomical structures nonadjacent to metal objects via edge-preserving filter. Then, the final prior image is acquired by restoring tissue information close to metallic implants. In Fig. 6, we can see that the proposed prior images, compared to TP-MAR priors, preserve more anatomical structures and significantly reduce residual artifacts. This is the main reason why our proposed MAR method outperforms TP-MAR methods.

One main limitation of our proposed MAR method comes from the fact that some bright artifacts around metal objects can be incorrectly incorporated into the final prior images as bone structures (as black solid arrow shows in Fig. 6), which can lead to fewer residual artifacts in the final corrected images. This is because the simple threshold technique used to identify the bone parts may lead to inaccurate bone structure. Therefore, advanced segmentation algorithms should be considered to address this limitation in the future. Another limitation is that we produce artificial sinogram via forward projecting the clinical images. The forward projection and FBP reconstruction have a low-pass filtering effect on final corrected images, which will lead to lower spatial resolution. Hence, our future work is to verify our proposed MAR method on real CT raw data. Third, due to the additional steps of forward projection, FBP reconstruction, filtering, segmentation and tissue-restoration, extra computation is needed for the proposed MAR method. The whole execution time of our proposed method is about 280 s, which is approximately 3.5 times of the LI-MAR based method. Nevertheless, the proposed algorithm can be accelerated via GPU-based technique [26–28] to fulfill the clinical requirements.

5. Conclusions

Metal artifacts can reduce image quality in CT images drastically. In this work, a novel prior-based

metal artifact reduction approach for metal artifact suppression has been proposed. Finding a good prior image is a crucial step in prior-based MAR methods. In our tests, we discover that residual artifacts and anatomical structures are two main factors determining the quality of the final prior image. The prior image resulting from our method produces more accurate results with almost no residual artifacts and much better preservation of anatomical structures. Experimental results in Figs 4 and 5 demonstrate our proposed MAR method's clinical potential via significant reduction of metal artifacts and successful restoration of tissue information, especially in the cases of large metallic implants. In the future, we will focus on addressing the limitations of our research described above. Furthermore, the method can be directly used to correct cone-beam CT (CBCT) images on a slice-by-slice basis. Alternatively, the proposed sinogram completion can be extended to work with 3D projection stack, making the proposed algorithm more applicable for CBCT images.

Acknowledgments

This work was partially supported by the National Natural Science Foundation of China (NSFC) through Grant No. 61201117 and No. 61301042, the Natural Science Foundation of Jiangsu province (NSFJ) through Grant No. BK2012189, the Key Technologies Research and Development Program of China through Grant No. 2012BA113B04 and the Special Funds for the Development of National Major Scientific Instruments and Equipment through Grant No. 2011YQ040082. The authors are very grateful for the CT images provided by the PET Center, Huashan Hospital, Fudan University.

References

[1] D.D. Robertson, P.J. Weiss, E.K. Fishman, D. Magid and P.S. Walker, Evaluation of CT techniques for reducing artifacts in the presence of metallic orthopedic implants, *Journal of Computer Assisted Tomography* **12** (1988), 236–241.
[2] W.A. Kalender, R. Hebel and J. Ebersberger, Reduction of CT artifacts caused by metallic implants, *Radiology* **164**(2) (1987), 576–577.
[3] J.W. Gu, L. Zhang, Z.Q. Chen, Y.X. Xing and Z.F. Huang, A method based on interpolation for metal artifacts reduction in CT images, *Journal of x-ray Science and Technology* **14** (2006), 11–19.
[4] J.W. Gu, L. Zhang, G.Q. Yu, Y.X. Xing and Z.Q. Chen, x-ray CT metal artifacts reduction through curvature based sinogram inpainting, *Journal of x-ray Science and Technology* **14** (2006), 73–82.
[5] W.J.H. Veldkamp, R.M.S. Joemai, A.J. van der Molen and J. Geleijns, Development and validation of segmentation and interpolation techniques in sinogram for metal artifact suppression in CT, *Medical Physics* **37**(2) (2010), 620–628.
[6] Y. Zhang, Y.F. Pu, J.R. Hu, Y. liu and J.L. Zhou, A new CT metal artifact reduction algorithm based on fractional-order sinogram inpainting, *Journal of x-ray Science and Technology* **19** (2011), 373–384.
[7] M. Bal and L. Spies, Metal artifact reduction in CT using tissue-class modeling and adaptive prefiltering, *Medical Physics* **33**(8) (2006), 2852–2859.
[8] E. Meyer, R. Raupach, M. Lell, B. Schmidt and M. Kachelrieß, Normalized metal artifact reduction (NMAR) in computed tomography, *Medical Physics* **37**(10) (2010), 5482–5493.
[9] D. Prell, Y. Kyrikou, M. Beister and W.A. Kalender, A novel forward projection-based metal artifact reduction method for flat-detector computed tomography, *Physics in Medicine Biology* **54**(21) (2009), 6575–6591.
[10] S. Karimi and P. Cosman, Segmentation of artifacts and anatomy in CT metal artifact reduction, *Medical Physics* **39**(10) (2012), 5857–5868.
[11] J. Wang, S. Wang, Y. Chen, J. Wu, J. Coatrieux and L. Luo, Metal artifact reduction in CT using fusion based prior image, *Medical Physics* **40**(8) (2013), 081903(8pp).
[12] X. Zhang, J. Wang and L. Xing, Metal artifact reduction in x-ray computed tomography (CT) by constrained optimization, *Medical Physics* **38** (2011), 701–711.
[13] E.Y. Sidky, C.M. Kao and X.H. Pan, Accurate image reconstruction from few-views and limited-angle data in divergent-beam CT, *Journal of x-ray Science and Technology* **14** (2006), 119–139.
[14] X. Zhang and L. Xing, Sequentially reweighted TV minimization for CT metal artifact reduction, *Medical Physics* **40**(7) (2013), 071907 (12pp).

[15] J. Choi, K.S. Kim, M.W. Kim, W. Seong and J.C. Ye, Sparsity driven metal part reconstruction for artifact removal in dental CT, *Journal of x-ray Science and Technology* **19** (2011), 457–475.
[16] D. Xia, J.C. Roeske, L. Yu, C.A. Pelizzari, A.J. Mundt and X. Pan, A hybrid approach to reducing computed tomography metal artifacts in intracavitary brachytherapy, *Brachytherapy* **4** (2005), 18–23.
[17] M. Oehler and T.M. Buzug, The k-MLEM algorithm: An iterative reconstruction technique for metal artifact reduction in CT images, *Advances in Medical Engineering* **114** (2007), 42–47.
[18] F.E. Boas and D. Fleischmann, Evaluation of two iterative techniques for reducing metal artifacts in computed tomography, *Radiology* **259** (2011), 894–902.
[19] Y. Zhang, H. Yan, X. Jia, J. Yang, S.B. Jiang and X. Mou, A hybrid metal artifact reduction algorithm for x-ray CT, *Medical Physics* **40**(4) (2013), 041910 (17pp).
[20] J. Besag, On the statistical-analysis of dirty pictures, *Journal of the Royal Statistical Society, Series B (Methodological)* **48**(3) (1986), 259–302.
[21] N. Karssemeijer, A stochastic-model for automated detection of calcifications in digital mammograms, *Lecture Notes in Computer Science* **511** (1991), 227–238.
[22] W. Zhuang, S.S. Gopal and T.J. Hebert, Numerical evaluation of methods for computing tomographic projections, *IEEE Transactions on Nuclear Science* **41** (1994), 1660–1665.
[23] P.J. La Rivière, J. Bian and P.A. Vargas, Penalized-likelihood sinogram restoration for computed tomography, *IEEE Transactions on Medical Imaging* **25**(8) (2006), 1022–1036.
[24] J.M. Boone and J.A. Seibert, An accurate method for computer-generating tungsten anode x-ray spectra from 30 to 140 Kv, *Medical Physics* **24**(11) (1997), 1661–1670.
[25] A. Mehranian, M.R. Ay, A. Rahmim and H. Zaidi, 3D prior image constrained projection completion for x-ray CT metal artifact reduction, *IEEE Transactions on Nuclear Science* **60**(5) (2013), 3318–3332.
[26] W. Pang, J. Qin, Y. Lu, Y. Xie, C. Chui and P. Heng, Accelerating simultaneous algebraic reconstruction technique with motion compensation using CUDA-enabled GPU, *International Journal of Computer Assisted Radiology and Surgery* **6**(2) (2011), 187–199.
[27] M. Beister, D. Prell, Y. Kyriakou and W.A. Kalender, GPU-accelerated metal artifact reduction (MAR) in FD-CT, *Proc SPIE7622, Medical Imaging 2010: Physics of Medical Imaging* **7622** (2010), 76223D (9pp).
[28] G.R. Yan, J. Tian, S.P. Zhu, Y.K. Dai and C.H. Qin, Fast cone-beam CT image reconstruction using GPU hardware, *Journal of x-ray Science and Technology* **16**(4) (2008), 225–234.